Resonating-valence-bond superconductor from small Fermi surface in twisted bilayer graphene

Jing-Yu Zhao[1] and Ya-Hui Zhang[1]

[1]*Department of Physics and Astronomy, Johns Hopkins University, Baltimore, Maryland 21218, USA*
(Dated: October 31, 2025)

Mechanism of superconductivity in twisted bilayer graphene (TBG) remains one of the central problems in strongly correlated topological systems. The most intriguing question is about the nature of the normal state: is the Cooper pair formed from small Fermi surface or large Fermi surface? In this work we point out the possibility of a symmetric pseudogap metal with small hole pockets, dubbed as second Fermi liquid (sFL). In the sFL phase at $\nu = -2 - x$, there is a two-component picture: two electrons mainly localize on the AA sites and form a paired singlet due to anti-Hund's coupling mediated by the optical phonon, while additional holes form small Fermi surfaces. The sFL phase corresponds to an intrinsically strongly interacting fixed point and violates the perturbative Luttinger theorem. We develop a unified framework to describe both a renormalized Fermi liquid (FL) and an sFL phase. We propose that the normal state of the TBG superconductor is the sFL phase, but it evolves toward the FL phase under increasing hole doping. The superconducting phase emerges from the sFL phase by transferring pairing of local moments to the mobile carriers. Interestingly, the superconducting gap can exhibit a nematic nodal p_x-pairing symmetry. This work provides, to our knowledge, the first unified theory that explains both the pseudogap metal above T_c and the two-gap nematic superconductivity below it.

Introduction The nature of superconductivity in magic-angle twisted bilayer graphene (TBG) [1–8] and in twisted multilayer graphene [9–12] remains a central puzzle in the study of correlated moiré materials [13–15]. Various pairing mechanisms have been proposed, including electron-phonon coupling [16–19], weak-coupling theories [20–25], and skyrmion-mediated superconductivity [26]. However, a comprehensive and well-established theory remains elusive. In particular, recent tunneling spectroscopy measurements [27, 28] have observed two distinct gaps in the superconducting phase. The smaller gap closes at the critical temperature T_c, while the larger gap survives above T_c, persisting as a pseudogap in the normal state. To our knowledge, no existing theory provides a unified explanation for both this two-gap structure and the associated pseudogap.

The existence of the pseudogap phase is reminiscent of high-T_c cuprates, where the pseudogap is widely believed to be associated with doped Mott insulator physics [29]. This naturally raises the question of whether superconductivity in TBG should also be understood as arising from doping a Mott insulator. However, applying a conventional Hubbard model to TBG is precluded by its fragile band topology [30–34]. As a result, many theoretical studies have focused on symmetry-breaking phases, such as inter-valley coherent (IVC) orders [35–39], often identified using momentum-space Hartree-Fock calculations within the continuum model [40]. Indeed, an intervalley Kekulé spiral (IKS) state – a specific IVC order with a non-zero wavevector $\mathbf{Q}$ [38, 41] – has been observed at filling $\nu = -2$ in STM experiments [28, 42, 43]. However, the relationship between this IKS state and superconductivity remains unclear. The lesson from cuprates suggests that the superconducting phase at finite hole doping may be disconnected from the symmetry-breaking order of the parent state at zero doping. Therefore, it remains worthwhile to explore theories of superconductivity that do not rely on these IVC orders.

Recently, the relevance of Mott physics and the formation of local moments in TBG has been increasingly recognized. On the experimental side, entropy measurements provide evidence for local moments, indicating Mott localization [44, 45]. On the theory side, local moments formation and Mott physics were studied using lattice models such as the topological heavy fermion model (THFM) [46–57] and non-local lattice models [58]. Alternatively, Mott physics can be understood using the ancilla framework [59] proposed by one of us [60]. Within this framework, it was demonstrated that a symmetric Mott state is possible at $\nu = -2$. Upon hole doping, the quasi-particles are still mainly from the f orbital instead of the c orbital[59, 61, 62]. Specifically, at filling $\nu = -2 - x$, this approach predicts a symmetric pseudogap metal with small hole pockets.

In this work, we propose that the normal state of the TBG superconductor is the pseudogap metal discussed above, which we dub the second Fermi liquid (sFL). The unique symmetry of TBG, $(U(1)_K \times U(1)_{K'} \times SU(2))/Z_2$, permits two distinct, symmetric Fermi liquid fixed points [63, 64]: a conventional Fermi liquid (FL) with a large Fermi surface, and an sFL phase with a small Fermi surface. At filling $\nu = -2-x$, the sFL phase is characterized by an emergent two-component picture: two electrons form localized moments on the AA sites, which are then paired into singlets by an on-site anti-Hund's coupling $J > 0$ mediated by optical phonons [65]. The additional carriers, with density x, form small hole pockets. We emphasize that this two-component picture is emergent and should not be confused with the naive decoupling of itinerant c and localized f orbitals in the THFM. Instead, both the mobile carriers and the local moments are from

the f orbital. It may be useful to view the f and c orbital as analogs of the copper (Cu) and oxygen (O) orbital in cuprate. It is well known that in hole doped cuprate the correct model must include both f orbital on Cu and c orbital on oxygen. But due to a large hybridization $\gamma c^\dagger f$, heavy fermion physics is irrelevant and the correct physics reduces to that of a one-orbital Hubbard model with only the f orbital. We suggest a similar picture for TBG. Conceptually, our sFL phase is closer to the fractionalized Fermi liquid (FL*) in one-orbital model of cuprate[60] than a naive Kondo decoupled phase.

The localized pairing, with an energy scale J, is consistent with experimental observations of a pseudogap, which as broad peaks in dI/dV at $\omega = \pm\Delta_{\text{PG}}$ [27, 28]. Due to strong repulsion U, these localized pairs are immobile and thus cannot directly lead to superconductivity. A key contribution of this work is to demonstrate that a superconducting dome emerges in proximity to the transition from the sFL to a renormalized FL phase, tuned by decreasing J or increasing doping x. Because the sFL state is beyond a Slater determinant description, we develop a parton mean-field theory based on the THFM to provide a unified framework for both the sFL and FL phases. Within this theory, approaching the FL phase from the sFL side triggers the condensation of a slave boson B below a coherence temperature T_{coh}. Below T_{coh}, this condensation allows the pre-formed pairing of the local moments to be transferred to the mobile carriers, opening a small superconducting gap on the small Fermi surfaces. The secondary superconducting pairing is characterized by a large real-space size and a nodal p_x pairing symmetry around the Fermi surface.

The spirit of our theory is similar to the Resonating Valence Bond (RVB) theory proposed for cuprates [66]. However, our model differs in key aspects: (I) Our parent state is a valence bond state without fractionalization, not an RVB spin liquid. (II) While both theories assume pre-formed pairs, their role differs. In conventional RVB theory[29], the spinon pairing in the parent state evolves directly into the superconducting pairing, while in our theory a secondary pairing is induced for the additional mobile carriers. Our mechanism also has conceptual similarities to the "molecular pairing" scenario in Ref. [67], but that analysis was restricted to a single Kondo impurity model. The physics of our theory aligns more closely with a purely f-orbital Hubbard model rather than with the simple Kondo model analysis presented in Ref. [67].

Model We use the THFM [46–52, 54–57, 68] description of the low energy bands of TBG:

$$H = H_0^{(c_1,c_2)} + H_0^{(c_1,f)} + H_{\text{int}}^{(f)} - \mu(N_c + N_f) , \quad (1)$$

which includes two dispersive bands, c_1 and c_2 described by $H_0^{(c_1,c_2)}$, and a Wannier flat band f. The c and f bands are hybridized as

$$H_0^{(c_1,f)} = \sum_{\mathbf{k},\mathbf{G}} f_{\mathbf{k}}^\dagger \gamma(\mathbf{k}+\mathbf{G}) c_{1,\mathbf{k}+\mathbf{G}} + \text{h.c.} , \quad (2)$$
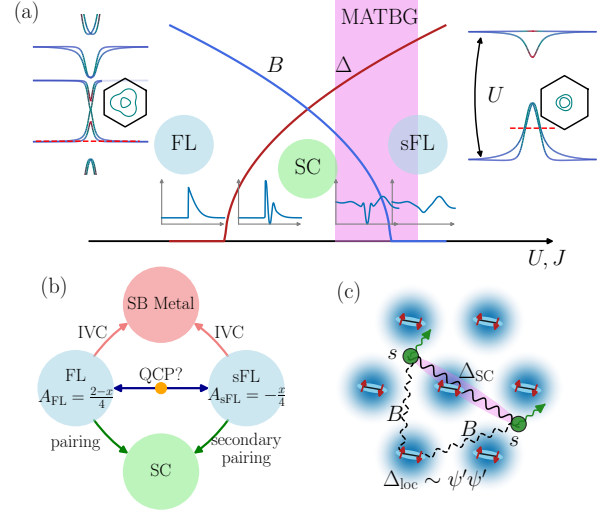

FIG. 1. (a) Schematic phase diagram illustrating the evolution from the sFL to the FL phase, for example, tuned by decreasing the anti-Hund's coupling J. The vertical axis denotes the temperature T. The left and right insets show the band structures and Fermi surfaces of the renormalized FL and sFL phases, respectively. Δ is the pairing of the local moments from the J term. B is the slave boson condensation, which sets a coherence temperature scale T_{coh}. In the phase diagram we also show illustration of tunneling spectrum. (b) Schematic illustration of the relationships among different phases. The FL and sFL phases correspond to two distinct symmetric fixed points. (c) Illustration of the RVB mechanism of superconductivity. We already have local pairing of spinons Δ_{loc}. Onset of the slave boson condensation B then induces resonance between the local pairing and two mobile carriers, leading to a superconducting pairing Δ_{SC} between the mobile carriers, which can be well separated in space.

where both $f_{\mathbf{k}}$ and $c_{1,\mathbf{k}}$ are eight-component spinors, collecting spin, valley, and orbital flavor: $f_{\mathbf{k}} = \{f_{\mathbf{k};\alpha}\}$ and $c_{1,\mathbf{k}} = \{c_{1,\mathbf{k};\alpha}\}$, with $\alpha = a\tau s$ formed by the orbital $a = \pm$, valley $\tau = K, K'$ and spin $s = \uparrow, \downarrow$. We choose a such that $f_{a=\pm;\tau s}$ has angular momentum $L = \pm 1$ around each AA site. Here the hybridization $\gamma(\mathbf{k}) = e^{-k^2\lambda^2/2}(\gamma\sigma_0 + v'_\star\tau_z(k_x\sigma_x + k_y\tau_z\sigma_y))s_0$, where σ_z, τ_z, s_z are Pauli matrices acting on the orbital, valley, and spin spaces. γ sets the scale of the remote band gap. For the f orbital, we include on-site interaction:

$$H_{\text{int}}^{(f)} = \frac{U}{2}\sum_i (n_{i;f} - 4 - \kappa\nu)^2 + \sum_i h_{i;J}^{(f)}, \quad (3)$$

where we also include an intra-site spin interaction term $h_{i;J}^{(f)}$ arising from electron–electron and electron-phonon couplings [54]. $h_{i;J}^{(f)}$ favors inter-valley spin-singlet pairing of the local moments as discussed in the Supplementary Material. We follow Ref. [55] to add a phenomenological parameter $-\kappa\nu$, which approximate the remaining repulsion interaction between c and f orbitals at Hartree level.
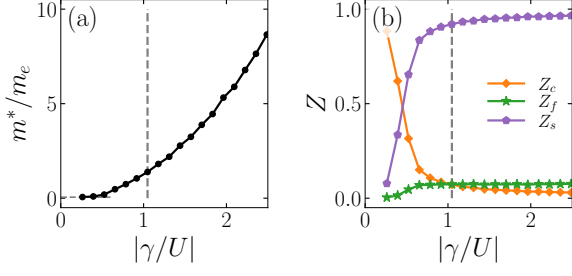
FIG. 2. (a) The effective mass m^*/m_e as a function of γ/U for the sFL phase at $\nu = -2.4$, where effective mass m^* is estimated by the zero energy density of state and m_e is the free electron mass. The horizontal dashed line marks the free electron mass of the c electron in the decoupled limit, with $m_0^*/m_e = 0.05$. (b) the quasi-particle weight of c, f and s fermions as a function of γ/U for $\nu = -2.4$. All the calculations are performed by varying U at fixed $\gamma = -26.184$ meV, with $w_0/w_1 = 0.8$, $\theta = 1.06°$ and $J = 6.0$ meV. The value of γ/U used in the main text is indicated by the vertical dashed lines in panels (a) and (b). The slave boson B is artificially set to 0 in the mean-field iteration to get the normal state of sFL.

We choose $\kappa = 0.8$ throughout the paper.

Simplified model at $\nu = -2 - x$ Different valences of the local f orbital are well separated on energy by the Hubbard U. We label the states with $n_{i;f} = 0, 1, 2, 3$ at each AA site i as holon, singlon, doublon and triplon. In the vicinity of the $\nu = -2$, the most relevant local configurations correspond to doublon, singlon and triplon. Due to $\gamma c^\dagger f$, there is a finite density of triplons even at $\nu = -2$ [61]. Following Ref. [61], we can consider a simplified model by projecting the original Hamiltonian into a restricted Hilbert space including only the 8 singlon state $|i; \alpha\rangle_s = f_{i;\alpha}^\dagger |0\rangle$, 28 doublon states $|i; \alpha\beta\rangle_d = f_{i;\alpha}^\dagger f_{i;\beta}^\dagger |0\rangle$ (with $\alpha < \beta$) and 56 triplon states $|i; \alpha\beta\gamma\rangle_t = f_{i;\alpha}^\dagger f_{i;\beta}^\dagger f_{i;\gamma}^\dagger |0\rangle$ (with $\alpha < \beta < \gamma$) at each AA site i.

The bilinear $P_G H_0 P_G$ term can be obtained by simply replacing $f_i \to P_G f_i P_G$, where P_G is the projection operator into the above restricted Hilbert space. The projected interaction term reads

$$P_G H_{\text{int}}^{(f)} P_G = \sum_i (E_s n_{i;s} + E_t n_{i;t} + h_{i;J}^{(f)} + \text{const.}) , \quad (4)$$

where $E_s = U/2 + U(2 + \kappa\nu)$ and $E_t = U/2 - U(2 + \kappa\nu)$ are on-site energy of singlon and triplon states. $n_{i;s}$, $n_{i;d}$ and $n_{i;t}$ are the density of singlon, doublon and triplon states.

Parton Mean field theory One convenient way to deal with the Hilbert space restriction is to use a parton theory. We imagine the singlon, doublon and triplon states are created by independent fermionic particles: $|i; \alpha\rangle_s = s_{i;\alpha}^\dagger |0\rangle$, $|i; \alpha\beta\rangle_d = \psi_{i;\alpha}'^\dagger \psi_{i;\beta}'^\dagger |0\rangle$ and $|i; \alpha\beta\gamma\rangle_t = t_{i;\alpha\beta\gamma}^\dagger |0\rangle$. Here s, ψ', t are fermionic operators.

The physical f operator in the restricted Hilbert space can be rewritten as

$$f_{i;\alpha} = \sum_\beta s_{i;\beta}^\dagger \psi_{i;\beta}' \psi_{i;\alpha}' + \sum_{\beta\gamma(\beta<\gamma)} t_{i;\alpha\beta\gamma} \psi_{i;\beta}'^\dagger \psi_{i;\gamma}'^\dagger . \quad (5)$$

At each site i, the partons always satisfy the local constraint $n_{i;s} + n_{i;\psi'}/2 + n_{i;t} = 1$, under which we have the relation $n_c + n_t - n_s = -x$ on average. We can think that s, ψ', t carry physical charge $+1, 0, -1$, respectively. The ψ' fermion is therefore a neutral spinon, which plays a role similar to the second ancillary fermion introduced in Ref. [60].

Mean field theory We can subsitute the above parton construction to the Hamiltonian and then do mean field decoupling. The spin interaction $h_{i;J}^{(f)}$ favors inter-valley singlet state between either $a\eta s$ and $\bar{a}\bar{\eta}\bar{s}$ (s-wave) or between $a\eta s$ and $a\bar{\eta}\bar{s}$ (d-wave). In the main text we focus on the time reversal invariant d-wave ansatz with $H_{J,\text{MF}} = -2J\Delta^* \sum_{i,a\eta s} s\psi_{i;a\bar{\eta}\bar{s}}' \psi_{i;a\eta s}'$, where $s = \pm$ for spin $\uparrow, \downarrow$ to indicate spin-singlet pairing. We use the notation $\bar{\alpha} = a\bar{\eta}\bar{s}$ for the pairing partner of $\alpha = a\eta s$, and when $\alpha = a\eta s$ is not used as a subscript, we use $\alpha = \pm$ to represent the spin sign according to $s = \uparrow, \downarrow$.

With Δ, we can describe the sFL phase with pairing of spinon ψ'. To describe a FL phase, we need to condense a slave boson, a bound state between electron and spinon $B \sim f_\alpha^\dagger \psi_\alpha'$. Together, we obtain the following mean-field Hamiltonian:

$$H_{\text{MF}} = H_0^{(c_1,c_2)} + H_{\text{MF}}^\Delta + H_{\text{MF}}^B + \sum_i (E_s - \lambda + \mu) n_{i;s}$$
$$+ \sum_i (E_t - \lambda - \mu) n_{i;t} - \mu N_c$$
$$H_{\text{MF}}^\Delta = \sum_{\mathbf{k},\mathbf{G}} c_{1,\mathbf{k}+\mathbf{G}}^\dagger \gamma(\mathbf{k}+\mathbf{G})(\Delta s_{-\mathbf{k}}^\dagger + \sqrt{3}\Delta^* t_{\mathbf{k}}) + \text{h.c.}$$
$$- 2J\Delta^* \psi_{-\mathbf{k}}' \psi_{\mathbf{k}}' + \text{h.c.}$$
$$H_{\text{MF}}^B = \sum_{\mathbf{k},\mathbf{G}} c_{1,\mathbf{k}+\mathbf{G}}^\dagger \gamma(\mathbf{k}+\mathbf{G})(B_s \psi_{\mathbf{k}}' + \Delta_t \psi_{-\mathbf{k}}'^\dagger) + \text{h.c.}$$
$$\sum_{\mathbf{k}} B_s' s_{\mathbf{k}}^\dagger \psi_{\mathbf{k}}' + \Delta_t' t_{\mathbf{k}}^\dagger \psi_{\mathbf{k}}' + \text{h.c.} .$$
$$(6)$$

Here $s_{-\mathbf{k}}$, $t_{\mathbf{k}}$ are eight-component spinors, $s_{-\mathbf{k}} = \{\alpha s_{-\mathbf{k};\bar{\alpha}}\}$, $t_{\mathbf{k}}^\dagger = \{t_{\mathbf{k};\alpha}^\dagger\}$, where $t_{\mathbf{k};\alpha} = \frac{1}{2\sqrt{3}} \sum_\beta \beta t_{\mathbf{k};\alpha\beta\bar{\beta}}$. And similar for $\psi_{\mathbf{k}}' = \{\psi_{\mathbf{k};\alpha}'\}$ and $\psi_{-\mathbf{k}}' = \{\alpha\psi_{-\bar{\alpha}}'\}$. Here the order parameters $B_s \propto \langle s_\beta^\dagger \psi_\beta' \rangle$, $\Delta_t \propto \langle t_\beta^\dagger \psi_\beta' \rangle$, $B_s' \propto \langle c_\alpha^\dagger \gamma_{\alpha\beta} \psi_\beta' \rangle$, $\Delta_t' \propto \beta \langle c_\alpha^\dagger \gamma_{\alpha\beta} \psi_{\bar\beta}'^\dagger \rangle$ and $\Delta \propto \alpha \langle \psi_{\bar\alpha}' \psi_\alpha' \rangle$ are determined self-consistently. An additional Lagrange multipler λ is introduced as $-\lambda(n_{i;s} + n_{i;t} + n_{i;\psi'}/2 - 1)$ to satisfy the local constraint on average. A chemical potential μ is introduced to satisfy the electron density constraint: $n_c + n_t - n_s = -x$.

The above ansatz make it possible to capture FL, sFL phase and superconductor (SC) phase in a unified framework. The corresponding ansatz are:
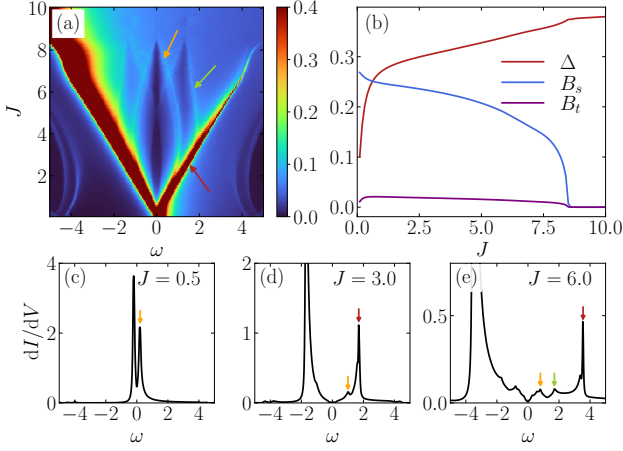
FIG. 3. Superconducting evolution as a function of the on-site spin interaction J, for $\theta = 1.06°$, $w_0/w_1 = 0.8$, $U = 25$ meV, $x = 0.4$ and $M = 0$. (a) The STM spectrum and (b) the order parameters for different value of J. The orange, red and green arrows mark the SC gap, the pseudogap and the inter-band gap. While the pseudogap always increase with increasing J, the SC gap first increases and then decreases as a function of J. (c) (d) and (e) show three different line cuts of STM at $J = 0.5$ meV, $J = 3.0$ meV and $J = 6.0$ meV, respectively.

- sFL: $\langle \Delta \rangle \neq 0$, $\langle B \rangle = 0$. There are hole pockets with Fermi surface volume (per spin and valley) $A_{FS} = -\frac{x}{4}$, mainly formed by the singlon $s^\dagger$ when x is relatively large.

- FL: $\langle \Delta \rangle = 0$, $\langle B \rangle \neq 0$. Now $f \sim s \sim \psi'$. The Fermi surface area per spin-valley flavor is $A_{FS} = \frac{2-x}{4}$.

- SC: $\langle \Delta \rangle \neq 0$, $\langle B \rangle \neq 0$. We can reach the SC phase from either the FL or sFL phase.

Correlated insulator and sFL We first consider the ansatz with $\Delta \neq 0$, but $B = 0$. At $\nu = -2$, this ansatz describes a mixed-valence Mott insulator [61]. Basically we start from a state with a singlet-paired doublon at each AA site, then on top we have finite densities of the triplon t and holes in the c bands, which form exciton pairs due to the γ coupling. These t and c excitations modify the Hubbard bands around Γ point. We focus on the lower Hubbard band, the excitation is dominated by a composite fermion $\psi_{i;\alpha} = -\frac{\sqrt{3}\alpha}{2}s^\dagger_{i;\bar{\alpha}} + \frac{1}{2}t_{i;\alpha}$ [61] at $k = 0$. But away from $k = 0$, the quasiparticle is dominated by $s^\dagger$.

At $\nu = -2 - x$, we have small hole pockets by moving the chemical potential to the lower Hubbard band (see the right inset of Fig. 1(a)). For each spin-valley flavor, there are two separate hole pockets arising from s_+, s_-. They are hybridized in the form $\sim (Me^{2i\phi(\mathbf{k})} + U\frac{v'_\star|\mathbf{k}|}{\gamma}e^{-i\phi(\mathbf{k})})s^\dagger_+ s_- + \text{h.c.}$, where M is the active band width and U is the Hubbard interaction. As a result of the hybridization, we always have two separate small hole
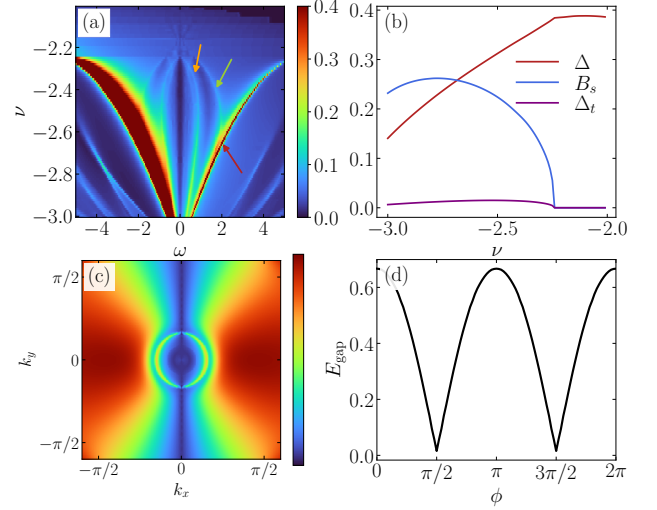

FIG. 4. Superconducting evolution as a function of the carrier density ν for twist angle $\theta = 1.06°$, $w_0/w_1 = 0.8$, $U = 25$ meV, $J = 6.0$ meV and $M = 0$. (a) The STM spectrum as for different charge densities. The orange, red and green arrows mark the SC gap, the pseudogap and the inter-band gap. (b) the order parameters for different value of ν. (c) and (d) show the nematic d-wave structure at a specific filling $\nu = -2.5$. (c) The pairing order parameter $|\Delta_{act,1}(\mathbf{k})|$, projected onto one of the lower Hubbard bands obtained by artificially setting $B_s = 0$. (d) The minimal single particle gap E_{gap} along different azimuth direction ϕ. The gap reaches its maximum along $\phi = 0, \pi$ directions and its minimum along $\phi \approx \pm\pi/2$ directions.

Fermi surfaces. Around each Fermi surface, the spinor in the basis of (s_+, s_-) shows a non-trivial winding. Later we will show that this structure is important for the nodal p_x-pairing of the small Fermi surfaces.

We emphasize that the sFL phase described here is beyond the naive decoupling limit between c and f at $\gamma/U = 0$. In Fig. 2 we show the evolution of the effective mass and the quasi-particle residue versus γ/U. When $\gamma/U \sim 1$ as used in our calculations relevant to TBG, m^* reaches order one of m_e and is roughly 20 times heavier than the bare itinerant c band. Moreover, the quasi-particle is dominated by the $s^\dagger$ fermion rather than c fermion. Clearly, both the mobile carriers and the local moments are mainly from the f orbital, so Kondo physics does not appear to be relevant.

Nematic superconductor from sFL: two-gap structure The sFL phase itself is expected to be stable when J is large. However, when J is reduced, the spinons can also gain coherence and the system transits to the FL phase. Therefore, we expect an onset of B when sFL phase is tuned towards the FL phase. In Fig. 3, we show the mean-field results by tuning the spin interaction J at a given doping level $x = 0.4$. Indeed, we find an onset of B when decreasing J, leading to a superconducting phase with both B and Δ non-zero. Note that when B is finite, the pairing of spinons (energy scale $J\Delta$) can induce a smaller superconducting pairing Δ_{SC} for the mo-

bile carriers and open a small gap on the Fermi surface. Fig. 3(a) shows the tunneling spectrum as a function of J. At large J, the SC is from the sFL phase, exhibiting two distinct gaps: a pseudogap Δ_{PG} labeled by the red arrow with the energy scale of $J\Delta$, and a superconducting gap Δ_{SC} labeled by the orange arrow. In this regime, the superconducting gap follows the trend of B. In the large J regime, we can also see another peak in tunneling spectrum labeled by the green arrow, which is from inter-band pairing. When decreasing J, the pseudogap and the SC gap merge together. At very small J, the SC should be understood as from the FL phase, then there is only one superconductor gap decided by $J\Delta$. Note the FL phase has a Kondo-like peak, and the superconductor gap simply splits it. An illustration of the band and Fermi surface of the FL phase can be found in Fig. 1(a).

To match the experimental phenomenology, we believe TBG is in the sFL side, so a relatively large J is required. We then fix $J = 6$ meV and study the doping dependence, as shown in Fig. 4. We find sFL is evolves toward FL phase also upon increasing x: B onsets at a small x and increases with x, while Δ decreases with x. For most of the doping range, they system remains on the sFL side, and both the pseudogap and the superconducting gap can be observed. Interestingly, the superconductor gap shows a dome-like structure and reaches the maximal value at optimal doping $x_p \approx 0.5$. In our theory, the pseudogap decreases monotonically with x.

Nodal p_x pairing Below the superconducting gap, the tunneling spectrum shows a V-shape around $\omega = 0$ and indicates a nodal pairing. In Fig. 4(c)(d), we show evidence of p_x pairing around each of the two Fermi surfaces of the sFL phase. Although the pairing of the spinon ψ' is always on-site, the transferred pairing on the small hole pockets acquires a p_x structure due to the winding of the spinor in the (s_+, s_-) basis around the Fermi surface. There are two nearby nodes from the two Fermi surfaces, and they may be gapped together by inter-pocket pairing if the pairing strength is sufficiently large.

Discussion We propose the normal state of TBG above T_c to be the sFL phase. Here $B = 0$, but the pairing gap of the spinon persists. We assume that there is fluctuation of B even above T_c, so the pairing gap from the spinon ψ' loses coherence, but is still visible as a broadened peak at $\Delta_{PG} \sim J\Delta$. Our theory thus offers a unified explanation of the pseudogap phase and the two-gap SC phase together. The major limitation of the current theory is that we ignored symmetry breaking orders such as the IKS state. Therefore, the current theory is more suitable in the overdoped region, but needs modification at small x to incorporate various IVC orders, which we leave for future work.

Conclusion In summary, we propose a theory for superconductivity in TBG that emerges from an unconventional, symmetric normal state. This state, which we dub the "second Fermi liquid" (sFL), features small hole pockets rather than the large Fermi surface of a conventional Fermi liquid. A key aspect of this sFL is the pre-existing pairing of local moments, mediated by optical phonons. Upon lowering the temperature, the preformed pairing is transferred to the mobile carriers, opening a smaller superconducting gap on the small Fermi surfaces. Our theory provides a unified explanation for recent experimental observations of a pseudogap and a two-gap structure in the superconducting state. The sFL normal state lies well beyond the usual Slater determinant framework, providing an example of an intrinsically strongly correlated metallic phase.

Note added: When finalizing the manuscript, we became aware of a preprint [69] that studied the single Kondo impurity model motivated by TBG. A specific limit of our sFL phase, the decoupling limit at $\gamma/U = 0$, was also discussed in [69]. However, our work mainly focuses on the $\gamma/U \sim 1$ region, where the sFL phase is beyond the Kondo decoupling description (see Fig. 2).

[1] Y. Cao, V. Fatemi, S. Fang, K. Watanabe, T. Taniguchi, E. Kaxiras, and P. Jarillo-Herrero, Unconventional superconductivity in magic-angle graphene superlattices, Nature **556**, 43 (2018).

[2] Y. Cao, V. Fatemi, A. Demir, S. Fang, S. L. Tomarken, J. Y. Luo, J. D. Sanchez-Yamagishi, K. Watanabe, T. Taniguchi, E. Kaxiras, R. C. Ashoori, and P. Jarillo-Herrero, Correlated insulator behaviour at half-filling in magic-angle graphene superlattices, Nature **556**, 80 (2018), arXiv:1802.00553.

[3] M. Yankowitz, S. Chen, H. Polshyn, Y. Zhang, K. Watanabe, T. Taniguchi, D. Graf, A. F. Young, and C. R. Dean, Tuning superconductivity in twisted bilayer graphene, Science **363**, 1059 (2019).

[4] X. Lu, P. Stepanov, W. Yang, M. Xie, M. A. Aamir, I. Das, C. Urgell, K. Watanabe, T. Taniguchi, G. Zhang, A. Bachtold, A. H. MacDonald, and D. K. Efetov, Superconductors, orbital magnets and correlated states in magic-angle bilayer graphene, Nature **574**, 653 (2019), arXiv:1903.06513.

[5] P. Stepanov, I. Das, X. Lu, A. Fahimniya, K. Watanabe, T. Taniguchi, F. H. L. Koppens, J. Lischner, L. Levitov, and D. K. Efetov, Untying the insulating and superconducting orders in magic-angle graphene, Nature **583**, 375 (2020), arXiv:1911.09198.

[6] Y. Cao, D. Rodan-Legrain, J. M. Park, N. F. Q. Yuan, K. Watanabe, T. Taniguchi, R. M. Fernandes, L. Fu, and P. Jarillo-Herrero, Nematicity and competing orders in superconducting magic-angle graphene, Science **372**, 264 (2021), arXiv:2004.04148.

[7] X. Liu, Z. Wang, K. Watanabe, T. Taniguchi, O. Vafek, and J. I. A. Li, Tuning electron correlation in magic-angle twisted bilayer graphene using Coulomb screening, Science **371**, 1261 (2021), arXiv:2003.11072.

[8] H. S. Arora, R. Polski, Y. Zhang, A. Thomson, Y. Choi, H. Kim, Z. Lin, I. Z. Wilson, X. Xu, J.-H. Chu, *et al.*, Superconductivity in metallic twisted bilayer graphene stabilized by wse2, Nature **583**, 379 (2020).

[9] J. M. Park, Y. Cao, K. Watanabe, T. Taniguchi, and P. Jarillo-Herrero, Tunable strongly coupled superconductivity in magic-angle twisted trilayer graphene, Nature **590**, 249 (2021).

[10] Z. Hao, A. Zimmerman, P. Ledwith, E. Khalaf, D. H. Najafabadi, K. Watanabe, T. Taniguchi, A. Vishwanath, and P. Kim, Electric field–tunable superconductivity in alternating-twist magic-angle trilayer graphene, Science **371**, 1133 (2021).

[11] J. M. Park, Y. Cao, L.-Q. Xia, S. Sun, K. Watanabe, T. Taniguchi, and P. Jarillo-Herrero, Robust superconductivity in magic-angle multilayer graphene family, Nature Materials **21**, 877 (2022).

[12] Y. Cao, J. M. Park, K. Watanabe, T. Taniguchi, and P. Jarillo-Herrero, Pauli-limit violation and re-entrant superconductivity in moiré graphene, Nature **595**, 526 (2021).

[13] E. Y. Andrei and A. H. MacDonald, Graphene bilayers with a twist, Nature materials **19**, 1265 (2020).

[14] E. Y. Andrei, D. K. Efetov, P. Jarillo-Herrero, A. H. MacDonald, K. F. Mak, T. Senthil, E. Tutuc, A. Yazdani, and A. F. Young, The marvels of moiré materials, Nature Reviews Materials **6**, 201 (2021).

[15] K. P. Nuckolls and A. Yazdani, A microscopic perspective on moiré materials, Nature Reviews Materials **9**, 460 (2024).

[16] F. Wu, Theory of Phonon-Mediated Superconductivity in Twisted Bilayer Graphene, Physical Review Letters **121**, 10.1103/PhysRevLett.121.257001 (2018).

[17] B. Lian, Z. Wang, and B. A. Bernevig, Twisted bilayer graphene: a phonon-driven superconductor, Physical review letters **122**, 257002 (2019).

[18] Y.-Z. Chou, Y.-P. Lin, S. Das Sarma, and R. M. Nandkishore, Superconductor versus insulator in twisted bilayer graphene, Physical Review B **100**, 115128 (2019).

[19] F. Wu, E. Hwang, and S. Das Sarma, Phonon-induced giant linear-in-t resistivity in magic angle twisted bilayer graphene: Ordinary strangeness and exotic superconductivity, Physical Review B **99**, 165112 (2019).

[20] G. Sharma, M. Trushin, O. P. Sushkov, G. Vignale, and S. Adam, Superconductivity from collective excitations in magic-angle twisted bilayer graphene, Physical Review Research **2**, 022040 (2020).

[21] H. Isobe, N. F. Q. Yuan, and L. Fu, Unconventional Superconductivity and Density Waves in Twisted Bilayer Graphene, Physical Review X **8**, 041041 (2018).

[22] D. V. Chichinadze, L. Classen, and A. V. Chubukov, Nematic superconductivity in twisted bilayer graphene, Physical Review B **101**, 224513 (2020).

[23] D. M. Kennes, Strong correlations and $d + id$ superconductivity in twisted bilayer graphene, Physical Review B **98**, 10.1103/PhysRevB.98.241407 (2018).

[24] J. González and T. Stauber, Kohn-Luttinger Superconductivity in Twisted Bilayer Graphene, Physical Review Letters **122**, 026801 (2019), arXiv:1807.01275 [cond-mat].

[25] Y.-Z. You and A. Vishwanath, Superconductivity from valley fluctuations and approximate SO(4) symmetry in a weak coupling theory of twisted bilayer graphene, npj Quantum Materials **4**, 16 (2019).

[26] E. Khalaf, S. Chatterjee, N. Bultinck, M. P. Zaletel, and A. Vishwanath, Charged skyrmions and topological origin of superconductivity in magic-angle graphene, Science advances **7**, eabf5299 (2021).

[27] J. M. Park, S. Sun, K. Watanabe, T. Taniguchi, and P. Jarillo-Herrero, Simultaneous transport and tunneling spectroscopy of moiré graphene: Distinct observation of the superconducting gap and signatures of nodal superconductivity (2025), arXiv:2503.16410.

[28] H. Kim, G. Rai, L. Crippa, D. Călugăru, H. Hu, Y. Choi, L. Kong, E. Baum, Y. Zhang, L. Holleis, K. Watanabe, T. Taniguchi, A. F. Young, B. A. Bernevig, R. Valentí, G. Sangiovanni, T. Wehling, and S. Nadj-Perge, Resolving Intervalley Gaps and Many-Body Resonances in Moiré Superconductor (2025), arXiv:2505.17200.

[29] P. A. Lee, N. Nagaosa, and X.-G. Wen, Doping a Mott insulator: Physics of high-temperature superconductivity, Reviews of Modern Physics **78**, 17 (2006), arXiv:0410445.

[30] H. C. Po, L. Zou, A. Vishwanath, and T. Senthil, Origin of Mott Insulating Behavior and Superconductivity in Twisted Bilayer Graphene, Physical Review X **8**, 031089 (2018), arXiv:1803.09742.

[31] G. Tarnopolsky, A. J. Kruchkov, and A. Vishwanath, Origin of Magic Angles in Twisted Bilayer Graphene, Physical Review Letter **122**, 106405 (2019), arXiv:2111.10018.

[32] J. Ahn, S. Park, and B.-j. Yang, Failure of Nielsen-Ninomiya Theorem and Fragile Topology in Two-Dimensional Systems with Space-Time Inversion Symmetry: Application to Twisted Bilayer Graphene at Magic Angle, Physical Review X **9**, 021013 (2019).

[33] P. J. Ledwith, E. Khalaf, and A. Vishwanath, Strong coupling theory of magic-angle graphene: A pedagogical introduction, Annals of Physics **435**, 168646 (2021), arXiv:2105.08858.

[34] Z.-d. Song, B. Lian, N. Regnault, and B. A. Bernevig, Twisted bilayer graphene. II. Stable symmetry anomaly, Physical Review B **103**, 205412 (2021).

[35] N. Bultinck, E. Khalaf, S. Liu, S. Chatterjee, A. Vishwanath, and M. P. Zaletel, Ground state and hidden symmetry of magic-angle graphene at even integer filling, Physical Review X **10**, 031034 (2020).

[36] Y. H. Kwan, G. Wagner, T. Soejima, M. P. Zaletel, S. H. Simon, S. A. Parameswaran, and N. Bultinck, Kekulé spiral order at all nonzero integer fillings in twisted bilayer graphene, Physical Review X **11**, 041063 (2021).

[37] D. E. Parker, T. Soejima, J. Hauschild, M. P. Zaletel, and N. Bultinck, Strain-induced quantum phase transitions in magic-angle graphene, Physical review letters **127**, 027601 (2021).

[38] G. Wagner, Y. H. Kwan, N. Bultinck, S. H. Simon, and S. Parameswaran, Global phase diagram of the normal state of twisted bilayer graphene, Physical review letters **128**, 156401 (2022).

[39] Z. Wang, G. Wagner, Y. H. Kwan, N. Bultinck, S. H. Simon, and S. A. Parameswaran, Putting a new spin on the incommensurate Kekulé spiral: from spin-valley locking and collective modes to fermiology and implications for superconductivity (2025).

[40] R. Bistritzer and A. H. MacDonald, Moiré bands in twisted double-layer graphene, Proc. Natl. Acad. Sci. **108**, 12233 (2011), arXiv:1009.4203.

[41] Y. H. Kwan, G. Wagner, T. Soejima, M. P. Zaletel, S. H. Simon, S. A. Parameswaran, and N. Bultinck, Kekulé Spiral Order at All Nonzero Integer Fillings in Twisted

Bilayer Graphene, Physical Review X **11**, 041063 (2021).

[42] H. Kim, Y. Choi, É. Lantagne-Hurtubise, C. Lewandowski, A. Thomson, L. Kong, H. Zhou, E. Baum, Y. Zhang, L. Holleis, *et al.*, Imaging inter-valley coherent order in magic-angle twisted trilayer graphene, Nature **623**, 942 (2023).

[43] K. P. Nuckolls, R. L. Lee, M. Oh, D. Wong, T. Soejima, J. P. Hong, D. Călugăru, J. Herzog-Arbeitman, B. A. Bernevig, K. Watanabe, *et al.*, Quantum textures of the many-body wavefunctions in magic-angle graphene, Nature **620**, 525 (2023).

[44] A. Rozen, J. M. Park, U. Zondiner, Y. Cao, D. Rodan-Legrain, T. Taniguchi, K. Watanabe, Y. Oreg, A. Stern, E. Berg, *et al.*, Entropic evidence for a pomeranchuk effect in magic-angle graphene, Nature **592**, 214 (2021).

[45] Y. Saito, F. Yang, J. Ge, X. Liu, T. Taniguchi, K. Watanabe, J. Li, E. Berg, and A. F. Young, Isospin pomeranchuk effect in twisted bilayer graphene, Nature **592**, 220 (2021).

[46] Z.-D. Song and B. A. Bernevig, Magic-Angle Twisted Bilayer Graphene as a Topological Heavy Fermion Problem, Physical Review Letter **129**, 047601 (2022), arXiv:2111.05865.

[47] D. Călugăru, M. Borovkov, L. L. H. Lau, P. Coleman, Z.-d. Song, and B. A. Bernevig, Twisted bilayer graphene as topological heavy fermion: II. Analytical approximations of the model parameters, Low Temperature Physics **49**, 640 (2023), arXiv:2303.03429.

[48] J. Yu, M. Xie, B. A. Bernevig, and S. Das Sarma, Magic-angle twisted symmetric trilayer graphene as a topological heavy-fermion problem, Physical Review B **108**, 035129 (2023).

[49] H. Hu, B. A. Bernevig, and A. M. Tsvelik, Kondo Lattice Model of Magic-Angle Twisted-Bilayer Graphene: Hund's Rule, Local-Moment Fluctuations, and Low-Energy Effective Theory, Physical Review Letters **131**, 026502 (2023).

[50] J. Herzog-Arbeitman, J. Yu, D. Călugăru, H. Hu, N. Regnault, C. Liu, O. Vafek, P. Coleman, A. Tsvelik, Z.-d. Song, and B. A. Bernevig, Topological Heavy Fermion Principle For Flat (Narrow) Bands With Concentrated Quantum Geometry, arXiv preprint , 1 (2024), arXiv:2404.07253.

[51] G.-D. Zhou, Y.-J. Wang, N. Tong, and Z.-D. Song, Kondo phase in twisted bilayer graphene, Physical Review B **109**, 045419 (2024).

[52] H. Hu, G. Rai, L. Crippa, J. Herzog-Arbeitman, D. Călugăru, T. Wehling, G. Sangiovanni, R. Valentí, A. M. Tsvelik, and B. A. Bernevig, Symmetric Kondo Lattice States in Doped Strained Twisted Bilayer Graphene, Physical Review Letters **131**, 166501 (2023), arXiv:2301.04673.

[53] Y.-Z. Chou and S. Das Sarma, Kondo Lattice Model in Magic-Angle Twisted Bilayer Graphene, Physical Review Letters **131**, 026501 (2023), arXiv:2211.15682.

[54] Y.-J. Wang, G.-D. Zhou, B. Lian, and Z.-D. Song, Electron phonon coupling in the topological heavy fermion model of twisted bilayer graphene, arXiv preprint , 1

(2024), arXiv:2407.11116.

[55] L. L. H. Lau and P. Coleman, Topological Mixed Valence Model for Twisted Bilayer Graphene, arXiv preprint , 1 (2023), arXiv:2303.02670.

[56] G. Rai, L. Crippa, D. Călugăru, H. Hu, F. Paoletti, L. de' Medici, A. Georges, B. A. Bernevig, R. Valentí, G. Sangiovanni, and T. Wehling, Dynamical Correlations and Order in Magic-Angle Twisted Bilayer Graphene, Physical Review X **14**, 031045 (2024).

[57] S. Youn, B. Goh, G.-D. Zhou, Z.-D. Song, and S.-S. B. Lee, Hundness in twisted bilayer graphene: correlated gaps and pairing, arXiv preprint **1**, 1 (2024), arXiv:2412.03108.

[58] P. J. Ledwith, J. Dong, A. Vishwanath, and E. Khalaf, Nonlocal Moments in the Chern Bands of Twisted Bilayer Graphene, arXiv preprint , 1 (2024), arXiv:2408.16761.

[59] J.-Y. Zhao, B. Zhou, and Y.-H. Zhang, Topological Mott localization and pseudogap metal in twisted bilayer graphene, Physical Review B **112**, 085107 (2025).

[60] Y.-H. Zhang and S. Sachdev, From the pseudogap metal to the Fermi liquid using ancilla qubits, Physical Review Research **2**, 023172 (2020), arXiv:2001.09159.

[61] J.-Y. Zhao, B. Zhou, and Y.-H. Zhang, Mixed valence Mott insulator and composite excitation in twisted bilayer graphene, arXiv preprint 10.48550/arXiv.2507.00139 (2025), arXiv:2507.00139.

[62] P. J. Ledwith, A. Vishwanath, and E. Khalaf, Exotic carriers from concentrated topology: Dirac trions as the origin of the missing spectral weight in twisted bilayer graphene, arXiv (2025), arXiv:2505.08779.

[63] Y.-H. Zhang and D. Mao, Spin liquids and pseudogap metals in the su (4) hubbard model in a moiré superlattice, Physical Review B **101**, 035122 (2020).

[64] H. Yang, H. Oh, and Y.-H. Zhang, Strong pairing from a small fermi surface beyond weak coupling: Application to La$_3$Ni$_2$O$_7$, Physical Review B **110**, 104517 (2024).

[65] C. Chen, K. P. Nuckolls, S. Ding, W. Miao, D. Wong, M. Oh, R. L. Lee, S. He, C. Peng, D. Pei, *et al.*, Strong electron–phonon coupling in magic-angle twisted bilayer graphene, Nature **636**, 342 (2024).

[66] P. W. Anderson, The resonating valence bond state in la2cuo4 and superconductivity, science **235**, 1196 (1987).

[67] Y.-J. Wang, G.-D. Zhou, S.-Y. Peng, B. Lian, and Z.-D. Song, Molecular pairing in twisted bilayer graphene superconductivity, Physical Review Letters **133**, 146001 (2024).

[68] H. Hu, Z.-D. Song, and B. A. Bernevig, Projected and Solvable Topological Heavy Fermion Model of Twisted Bilayer Graphene, arXiv preprint , 225 (2025), arXiv:2502.14039.

[69] Y.-J. Wang, G.-D. Zhou, H. Jung, S. Youn, S.-S. B. Lee, and Z.-D. Song, Solution to a Quantum Impurity Model for Moiré Systems: Fermi Liquid, Pairing, and Pseudogap (2025), arXiv:2510.23604.

[70] T. Senthil, S. Sachdev, and M. Vojta, Fractionalized fermi liquids, Physical review letters **90**, 216403 (2003).

[71] T. Senthil and M. P. Fisher, Z_2 gauge theory of electron fractionalization in strongly correlated systems, Physical Review B **62**, 7850 (2000).

Appendix A: THFM with on-site spin interactions

We now present the full expression of the THFM as introduced in Eq. (1).

$$H = H_0^{(c_1,c_2)} + H_0^{(c_1,f)} + H_{\text{int}}^{(f)} - \mu(N_c + N_f), \tag{A1}$$

which includes two dispersive bands, c_1 and c_2 described by $H_0^{(c_1,c_2)}$, and a flat band f described by the interaction $H_{\text{int}}^{(f)}$. f has a Wannier orbital well localized on the triangular lattice AA sites. The c and f orbitals are hybridized through $H_0^{(c_1,f)}$. We use f_i and $c_{1,\mathbf{k}}$, $c_{2,\mathbf{k}}$ as eight-component spinors, collecting spin, valley, and orbital flavor: $f_i = \{f_{i;\alpha}\}$, $c_{1,\mathbf{k}} = \{c_{1,\mathbf{k};\alpha}\}$ and $c_{2,\mathbf{k}} = \{c_{2,\mathbf{k};\alpha}\}$, with $\alpha = a\tau s$ formed by the orbital $a = \pm$, valley $\tau = K, K'$ and spin $s = \uparrow, \downarrow$. Here we choose the orbital index $a = \pm$ such that $f_{a=\pm;\tau s}$ has angular momentum $L = \pm 1$ around each AA site. We use σ_z, τ_z, s_z to denote the Pauli matrices acting on the orbital, vally and spin spaces, respectively. Here

$$H_0^{(c_1,c_2)} = v_\star \sum_{\mathbf{k}} \left(c_{1,\mathbf{k}}^\dagger \tau_z \left(k_x \sigma_0 + i k_y \sigma_z \right) c_{2,\mathbf{k}} + \text{h.c.} \right) + \sum_{\mathbf{k}} c_{2,\mathbf{k}}^\dagger M \sigma_x c_{2,\mathbf{k}}, \tag{A2}$$

$$H_0^{(c_1,f)} = \frac{1}{\sqrt{N}} \sum_{\mathbf{k},i} e^{i\mathbf{k}\cdot\mathbf{R}_i - \frac{k^2\lambda^2}{2}} f_i^\dagger \left(\gamma \sigma_0 + v_\star' \tau_z \left(k_x \sigma_x + k_y \tau_z \sigma_y \right) \right) c_{1,\mathbf{k}} + \text{h.c.}, \tag{A3}$$

$$H_{\text{int}}^{(f)} = U/2 \sum_i (n_{i;f} - 4 - \kappa\nu)^2 + \sum_i h_{i;J}^{(f)}, \tag{A4}$$

where the band width of the itinerant c_1, c_2 band $v_\star|\mathbf{K}|$ is always the largest energy scale in the model, M characterizes the Γ-point splitting of the active flat bands in TBG, and γ characterizes the remote band gap at the Γ point. We choose a set of parameters from [47, 67] for a twist angle $\theta = 1.06°$ near the optimal doping, where we set $\gamma = -26.184$ meV, $v_\star = -4.335$ eV Å, $v_\star' = 1.633$ eV Å and $\lambda = 0.339$ (in units of the moiré lattice constant). A phenomenological parameter $\kappa = 0.8$ is introduced in the Hubbard interaction to account for the coulomb repulsive between c and f electrons. The value of the active band width M mainly affects the nodal structure of the pairing state and is discussed in detail in Appendix D. We take $M = 0$ in the main text calculations.

1. Spin interaction

Here we follow Ref [67] to include two different kinds of effective interactions between the f orbitals within each AA site.

$$h_{i;J}^{(f)} = h_{i;J_A}^{(f)} + h_{i;J_H}^{(f)}, \tag{A5}$$

where

$$h_{i;J_A}^{(f)} = -\frac{J_A}{2} \sum_{\alpha\eta\beta s s'} f_{i;\beta\bar{\eta}s}^\dagger f_{i;\alpha\eta s'}^\dagger f_{i;\beta\bar{\eta}s'} f_{i;\alpha\eta s} - \frac{J_A}{2} \sum_{\alpha\eta s s'} f_{i;\alpha\bar{\eta}s}^\dagger f_{i;\bar{\alpha}\bar{\eta}s'}^\dagger f_{i;\bar{\alpha}\bar{\eta}s'} f_{i;\alpha\eta s} \tag{A6}$$

is anti-Hund's coupling induced by the electron-phonon interaction. And

$$h_{i;J_H}^{(f)} = \sum_{\alpha s s'} \sum_{\eta_{1,2,3,4}} \delta_{\eta_1+\eta_2,\eta_3+\eta_4} \frac{J_H}{2} f_{i;(\alpha\eta_1)\eta_1 s}^\dagger f_{i;(\alpha\eta_2)\eta_2 s'}^\dagger f_{i;(\alpha\eta_3)\eta_3 s'} f_{i;(\alpha\eta_4)\eta_4 s}$$

$$+ \sum_{\alpha s s'\eta_1,\eta_2} \left[\frac{J_H'}{2} f_{i;(\alpha\eta_1)\eta_1 s}^\dagger f_{i;(\alpha\bar{\eta}_1)\bar{\eta}_1 s'}^\dagger f_{i;(\bar{\alpha}\bar{\eta}_2)\bar{\eta}_2 s'} f_{i;(\bar{\alpha}\eta_4)\eta_4 s} + \frac{J_H'}{2} f_{i;(\alpha\eta_1)\eta_1 s}^\dagger f_{i;(\bar{\alpha}\eta_2)\eta_2 s'}^\dagger f_{i;\bar{\alpha}\eta_2 s'} f_{i;(\alpha\eta_1)\eta_1 s} \right. \tag{A7}$$

$$\left. + \frac{J_H'}{2} f_{i;(\alpha\eta_1)\eta_1 s}^\dagger f_{i;(\bar{\alpha}\eta_2)\eta_2 s'}^\dagger f_{i;(\alpha\eta_1)\eta_1 s'} f_{i;(\bar{\alpha}\eta_2)\eta_2 s} \right].$$

is a Hund's coupling between different sublattices induced by the Coulomb interaction.

The spin interaction can be solved exactly for the singly, doubly and triply occupied states, respectively. The singly occupied states do not receive energy from the intra-site spin interaction, and the triply occupied state is not

important in the doping regime $\nu = -2 - x$ we studied here. Therefore, here we focus on the doubly occupied states, which serves as the parent state. In combination of the above two terms, the on-site ground state is found to be an inter-valley singlet pairing state between either $a\eta s$ and $\bar{a}\bar{\eta}\bar{s}$, or between $a\eta s$ and $a\bar{\eta}\bar{s}$, depending on the detailed parameters. For $J_H' = J_H/3$, the lowest energy state is found to be an $L_z = 0$ state

$$|\Delta_{i;s}\rangle = \frac{1}{2} \left(f_{i;+K\uparrow}^\dagger f_{i;-K'\downarrow}^\dagger - f_{i;+K\downarrow}^\dagger f_{i;-K'\uparrow}^\dagger + f_{i;-K\uparrow}^\dagger f_{i;+K'\downarrow}^\dagger - f_{i;-K\downarrow}^\dagger f_{i;+K'\uparrow}^\dagger \right) |0\rangle, \tag{A8}$$

for $J_H < J_A/2$. In contrast, when $J_A < J_H < 3J_A/2$, the lowest-energy manifold is twofold degenerate, consisting of the states

$$|\Delta_{i;d_1}\rangle = \frac{1}{\sqrt{2}} (f_{i;+K\uparrow}^\dagger f_{i;+K'\downarrow}^\dagger - f_{i;+K\downarrow}^\dagger f_{i;+K'\uparrow}^\dagger)|0\rangle$$
$$|\Delta_{i;d_2}\rangle = \frac{1}{\sqrt{2}} (f_{i;-K\uparrow}^\dagger f_{i;-K'\downarrow}^\dagger - f_{i;-K\downarrow}^\dagger f_{i;-K'\uparrow}^\dagger)|0\rangle. \tag{A9}$$

with angular momentum $L = \pm 2$, respectively. In our mean-field calculation, we will always assume an equal weight superposition of these two degenerate state $|\Delta_{i;d}\rangle = \frac{1}{\sqrt{2}}(|\Delta_{i;d_1}\rangle + |\Delta_{i;d_2}\rangle)$, which satisfy the $C_{2z}T$ symmetry, but breaks the C_3 symmetry. It should be selected by a small finite heterostrain.

Appendix B: Details on the mean field theory calculation

1. Slave particle theory

To analytically treat the restricted Hilbert space which includes only singlon, doublon and triplon states of f orbital, we propose the following parton construction:

$$f_{i;\alpha}^\dagger |0\rangle \rightarrow s_{i;\alpha}^\dagger |0\rangle$$
$$f_{i;\alpha}^\dagger f_{i;\beta}^\dagger |0\rangle \rightarrow \psi_{i;\alpha}'^\dagger \psi_{i;\beta}'^\dagger |0\rangle \tag{B1}$$
$$f_{i;\alpha}^\dagger f_{i;\beta}^\dagger f_{i;\gamma}^\dagger |0\rangle \rightarrow t_{i;\alpha\beta\gamma}^\dagger |0\rangle$$

where s, ψ' and t are all fermions which satisfy a local constraint:

$$n_{i;s} + n_{i;\psi'}/2 + n_{i;t} = 1, \tag{B2}$$

at every AA site i. Here $n_{i;s}, n_{i;\psi'}$ and $n_{i;t}$ are the total particle numbers of s, ψ' and t at each site i. The constraint introduces a gauge redundancy $s_i \rightarrow s_i e^{2i\varphi_i}, \psi_i' \rightarrow \psi_i' e^{i\varphi_i}$ and $t_i \rightarrow t_i e^{2i\varphi_i}$.

We now write down the projected Hamiltonian $P_G H_0 P_G$ in terms of these partons. First, the original f_i fermion operator is written as

$$f_{i;\alpha} = \sum_\beta s_{i;\beta}^\dagger \psi_{i;\beta}' \psi_{i;\alpha}' + \sum_{\beta,\gamma(\beta<\gamma)} t_{i;\alpha\beta\gamma} \psi_{i;\beta}'^\dagger \psi_{i;\gamma}'^\dagger, \tag{B3}$$

The bilinear part of the Hamiltonian $P_G H_0 P_G$ can be obtained by directly replacing the $f_{i;\alpha}^\dagger$ operators with the expression above.

The interaction energy (A4) are composed of two part. For the Hubbard interaction part, we write it down exactly in the restricted Hilbert space for each valences f^{1+}, f^{2+}, f^{3+} as $E_{1+}^f = (3 + \kappa\nu)^2 U/2$, $E_{2+}^f = (2 + \kappa\nu)^2 U/2$ and $E_{3+}^f = (1 + \kappa\nu)^2 U/2$. The spin interaction is only meaningful for the doublon represented by ψ'. We thus replace the f fermions in Eqs. (A6) and (A7) with ψ' as $h_{i;J}^{(f)} \rightarrow h_{i;J}^{(\psi')}$. We will keep the full interaction $h_{i;J}^{(\psi')}$ for now and leave it for the mean-field calculation later. With the chemical potential μ and a Lagrange multipler, the onsite energy of each parton is:

$$P_G(\sum_i H_{i;\text{int}}^{(f)} - \mu N_f)P_G - \lambda_0 \sum_i (n_{i;} + n_{i;\psi'}/2 + n_{i;t} - 1)$$
$$= (E_s + \mu - \lambda) \sum_{i;\alpha} s_{i;\alpha}^\dagger s_{i;\alpha} - \frac{1}{2}\lambda \sum_{i;\alpha} \psi_{i;\alpha}'^\dagger \psi_{i;\alpha}' + (E_t - \mu - \lambda) \sum_{i;\alpha\beta\gamma} t_{i;\alpha\beta\gamma}^\dagger t_{i;\alpha\beta\gamma} + \sum_i h_{i;J}^{(\psi')} + \cdots. \tag{B4}$$

where $\cdots$ represents the spin interaction within the triplon subspace, which will be omitted, as well as an overall constant. We also shift the Lagrange multiplier to $\lambda_0 = E^f_{2+} - 2\mu + \lambda$ and

$$E_s = E^f_{1+} - E^f_{2+} = U/2 + U(2 + \kappa\nu), \tag{B5}$$

$$E_t = E^f_{3+} - E^f_{2+} = U/2 - U(2 + \kappa\nu). \tag{B6}$$

In summary, the projected Hamiltonian written in terms of the partons is:

$$\begin{aligned}
P_G H P_G =& H_0^{(c_1,c_2)} - \mu N_c + \frac{1}{\sqrt{N}} \sum_{\mathbf{k},\mathbf{G},i} e^{i\mathbf{k}\cdot\mathbf{R}_i} c^\dagger_{1,\mathbf{k}+\mathbf{G}} \gamma(\mathbf{k}+\mathbf{G}) \left(\sum_\beta s^\dagger_{i;\beta} \psi'_{i;\beta} \psi'_{i;\alpha} + \sum_{\beta\gamma(\beta<\gamma)} t_{i;\alpha\beta\gamma} \psi'^\dagger_{i;\beta} \psi'^\dagger_{i;\gamma} \right) + \text{h.c.} \\
& + (E_s + \mu - \lambda) \sum_{i,\alpha} s^\dagger_{i;\alpha} s_{i;\alpha} - \frac{1}{2}\lambda \sum_{i,\alpha} \psi'^\dagger_{i;\alpha} \psi'_{i;\alpha} + (E_t - \mu - \lambda) \sum_{i,\alpha} t^\dagger_{i;\alpha} t_{i;\alpha} + \sum_i h^{(\psi')}_{i;J} + \text{const.},
\end{aligned} \tag{B7}$$

2. Mean field theory

a. Spin interaction

In the mean-field calculation, we can decouple the full spin Hamiltonian Eq. (A5) into both the s-wave and d-wave channels and solve the self-consistent equation. However, the f_i orbitals are localized on the AA site and the intra-site spin Hamiltonian can be solved exactly. With knowledge of the ground state at different parameter regime, Here we directly assume that the pairing channel is either the s-wave state $|\Delta_{i;s}\rangle$ or $C_{2z}T$ symmetric d-wave state $|\Delta_{i;d}\rangle$ and consider the mean-field Hamiltonian

$$H^s_{J,\text{MF}} = -2J_s \sum_{i;a\eta s} \Delta^*_s s \psi'_{i;\bar{a}\bar{\eta}\bar{s}} \psi'_{i;a\eta s} + \text{h.c.} , \tag{B8}$$

for the s-wave pairing, where $\Delta_s = s\langle \psi'_{\bar{a}\bar{\eta}\bar{s}} \psi'_{a\eta s} \rangle$, $s = \pm$ is the spin singlet sign. And we consider

$$H^d_{J,\text{MF}} = -2J_d \sum_{i;a\eta s} \Delta^*_d s \psi'_{i;a\bar{\eta}\bar{s}} \psi'_{i;a\eta s} + \text{h.c.} , \tag{B9}$$

for the d-wave pairing, with $\Delta_d = s\langle \psi'_{a\bar{\eta}\bar{s}} \psi'_{a\eta s} \rangle$. Here the value of J_s or J_d is generally a linear combination of the microscopic parameters J_A and J_H.

Motivated by the experimental observation of a V-shaped spectrum, we choose the d-wave pairing channel as the pairing of the spinon ψ' in the main text. Because we are not interested in the competition between the d wave and s wave ansatz, we can keep only one parameter $J = J_d$ for the spin interaction. From now on, we use Eq. (B9) and omit the subscript d for simplicity. Since each flavor $f_{i;\alpha}$ is paired uniquely with another flavor $f_{i;\bar{\alpha}}$ in $|\Delta_{d;i}\rangle$, we define

$$\bar{\alpha} = a\bar{\tau}\bar{s} \quad \text{for} \quad \alpha = a\tau s. \tag{B10}$$

And for $\alpha = a\eta s$, when α is not used as a subscript, we let α itself represent a sign $\pm$, determined by the spin $s = \uparrow, \downarrow$.

b. Hybridization term

For the hybridization term $c^\dagger_{\mathbf{k};\alpha} \gamma(\mathbf{k})_{\alpha\beta} f_{i;\beta}$, we consider two different kinds of mean field channels. First when J term is large, the $\psi'_{i;\alpha}$ particle would fall into a pair instability with $\langle \psi'_{i;\beta} \psi'_{i;\alpha} \rangle = \alpha\Delta\delta_{\alpha\bar{\beta}}$. We get the pairing mean-field channel as

$$\begin{aligned}
P_G c^\dagger_{\mathbf{k};\lambda} \gamma(\mathbf{k})_{\lambda\alpha} f_{i;\alpha} P_G =& c^\dagger_{\mathbf{k};\lambda} \gamma(\mathbf{k})_{\lambda\alpha} \left(\sum_\beta s^\dagger_{i;\beta} \psi'_{i;\beta} \psi'_{i;\alpha} + \sum_{\beta\gamma(\beta<\gamma)} t_{i;\alpha\beta\gamma} \psi'^\dagger_{i;\beta} \psi'^\dagger_{i;\gamma} \right) \\
& \sim c^\dagger_{\mathbf{k};\lambda} \gamma(\mathbf{k})_{\lambda\alpha} \left(\alpha\Delta s^\dagger_{i;\bar{\alpha}} + \Delta^* \sum_{\beta(\beta<\bar{\beta})} \beta t_{i;\alpha\beta\bar{\beta}} \right) .
\end{aligned} \tag{B11}$$

In the above decoupling of $c^\dagger \gamma f$, there will be another term $\sim \langle c^\dagger \gamma s + t^\dagger \gamma c \rangle \psi' \psi'$. We take this term as small compared to the spin induced pairing Eq. (B9) and omitted. Note that only 8 independent fermions of the 56 triplon t fermions are coupled to the other fermions in the mean-field level. We therefore introduce a recombined triplon fermion as: $t_{i;\alpha} = \frac{1}{2\sqrt{3}} \sum_\beta \beta t_{i;\alpha\beta\bar{\beta}}$. We use the same notation t here for the recombined triplon and distinguish it with the original triplon by the number of subscript. In terms of this new triplon,

$$P_G f_{i;\alpha} P_G = \alpha \Delta s^\dagger_{i;\bar{\alpha}} + \sqrt{3}\Delta^* t_{i;\alpha} , \tag{B12}$$

which recovers the result of Ref. [61].

The other possible mean-field channel is the hybridization between charge neutral ψ' and charged particles s, t and c_1,

$$
\begin{aligned}
\sum_{\alpha,\lambda} P_G c^\dagger_{\mathbf{k};\lambda} \gamma(\mathbf{k})_{\lambda\alpha} f_{i;\alpha} P_G = & \sum_{\alpha,\lambda} c^\dagger_{\mathbf{k};\lambda} \gamma(\mathbf{k})_{\lambda\alpha} \Big(\sum_\beta s^\dagger_{i;\beta} \psi'_{i;\beta} \psi'_{i;\alpha} + \sum_{\beta\gamma} t_{i;\alpha\beta\gamma} \psi'^\dagger_{i;\beta} \psi'^\dagger_{i;\gamma} \Big) \\
\sim & \sum_{\alpha,\beta,\lambda} \langle c^\dagger_{\mathbf{k};\lambda} \gamma(\mathbf{k})_{\lambda\alpha} \psi'_{i;\alpha} \rangle s^\dagger_{i;\beta} \psi'_{i;\beta} + \sum_{\alpha,\beta,\lambda} c^\dagger_{\mathbf{k};\lambda} \gamma(\mathbf{k})_{\lambda\alpha} \psi'_{i;\alpha} \langle s^\dagger_{i;\beta} \psi'_{i;\beta} \rangle \\
& + \frac{1}{\sqrt{3}} \sum_{\alpha,\beta,\lambda} \alpha \langle c^\dagger_{\mathbf{k};\lambda} \gamma(\mathbf{k})_{\lambda\alpha} \psi'^\dagger_{i;\bar{\alpha}} \rangle \psi'^\dagger_{i;\beta} t_{i;\beta} + \frac{1}{\sqrt{3}} \sum_{\alpha,\beta,\lambda} \alpha c^\dagger_{\mathbf{k};\lambda} \gamma(\mathbf{k})_{\lambda\alpha} \psi'^\dagger_{i;\bar{\alpha}} \langle \psi'^\dagger_{i;\beta} t_{i;\beta} \rangle ,
\end{aligned}
\tag{B13}
$$

where we have assumed $\sum_\lambda \langle c^\dagger_{\mathbf{k};\lambda} \gamma(\mathbf{k})_{\lambda\alpha} \psi'^\dagger_{i;\beta} \rangle \propto \alpha \delta_{\alpha,\bar{\beta}}$. This relies on a strong pairing Δ such that only the 8 tripons introduced above are important.

We can now write down the full mean-field Hamiltonian as

$$
\begin{aligned}
H_{\mathrm{MF}} = & H_0^{(c_1,c_2)} \\
& + \sum_{\mathbf{k},\mathbf{G},\alpha\beta} c^\dagger_{1,\mathbf{k}+\mathbf{G};\alpha} \gamma(\mathbf{k}+\mathbf{G})_{\alpha\beta} (\alpha\Delta s^\dagger_{-\mathbf{k};\bar{\alpha}} + \sqrt{3}\Delta^* t_{\mathbf{k};\alpha}) + \mathrm{h.c.} - 2J \sum_{\mathbf{k},\alpha} \Delta^* \alpha \psi'_{-\mathbf{k};\bar{\alpha}} \psi'_{\mathbf{k};\alpha} + \mathrm{h.c.} \\
& + \sum_{\mathbf{k},\mathbf{G},\alpha\beta} c^\dagger_{1,\mathbf{k}+\mathbf{G};\alpha} \gamma(\mathbf{k}+\mathbf{G})_{\alpha\beta} (B_s \psi'_{\mathbf{k};\alpha} + \alpha\Delta_t \psi'^\dagger_{-\mathbf{k};\bar{\alpha}}) + \mathrm{h.c.} + \sum_{\mathbf{k};\alpha} (B'_s s^\dagger_{\mathbf{k};\alpha} \psi'_{\mathbf{k};\alpha} + \Delta'_t t^\dagger_{\mathbf{k};\alpha} \psi'_{\mathbf{k};\alpha}) + \mathrm{h.c} \\
& + (E_s + \mu - \lambda) \sum_{i;\alpha} s^\dagger_{i;\alpha} s_{i;\alpha} - \frac{1}{2}\lambda \sum_{i;\alpha} \psi'^\dagger_{i;\alpha} \psi'_{i;\alpha} + (E_t - \mu - \lambda) \sum_{i;\alpha} t^\dagger_{i;\alpha} t_{i;\alpha} + \mathrm{const.},
\end{aligned}
\tag{B14}
$$

where the order parameters are solved iteratively as:

$$
\begin{aligned}
\Delta = & \frac{1}{N} \sum_{\mathbf{k}} \alpha \langle \psi'_{-\mathbf{k};\bar{\alpha}} \psi'_{\mathbf{k};\alpha} \rangle , \\
B_s = & 7\alpha_B \frac{1}{N} \sum_{\mathbf{k}} \langle s^\dagger_{\mathbf{k};\alpha} \psi'_{\mathbf{k};\alpha} \rangle , \\
B'_s = & 7\alpha_B \frac{1}{N} \sum_{\mathbf{k};\alpha} \langle c^\dagger_{1;\mathbf{k};\alpha} \gamma_{\alpha\beta} \psi'_{\mathbf{k};\beta} \rangle , \\
\Delta_t = & 2\sqrt{3}\alpha_B \frac{1}{N} \sum_{\mathbf{k}} \langle t^\dagger_{\mathbf{k};\alpha} \psi'_{\mathbf{k};\alpha} \rangle , \\
\Delta'_t = & 2\sqrt{3}\alpha_B \frac{1}{N} \sum_{\mathbf{k};\alpha} \beta \langle c^\dagger_{1;\mathbf{k};\alpha} \gamma_{\alpha\beta} \psi'^\dagger_{\mathbf{k};\bar{\beta}} \rangle ,
\end{aligned}
\tag{B15}
$$

where N is the total number of AA site in our calculation. The coefficient in front of B_s, B'_s and Δ_t, Δ'_t are determined by index counting. An additional phenomenological coefficient $\alpha_B < 1$ is introduced to control the convergence of mean-field calculation. To validate an α_B smaller than the unity, we can consider the infinite J limit, where the double occupied state of f should be further projected to a subspace with lower spin energy. The coefficient will be much smaller in this limit. In reality, we consider a finite J term and should as a result take a finite α_B. In reality, we take $\alpha_B = 1/2$ and find good convergence. We note this is one limitation of mean-field calculation and leave further validation to variational Monte Carlo calculation calculation.

Finally, in extracting the spectrum function at the mean-field level, we rewrite the f fermion as:

$$P_G f_{i;\alpha} P_G = \Delta \alpha s^\dagger_{i;\bar{\alpha}} + \sqrt{3}\Delta^* t_{i;\alpha} + B_s \psi'_{i;\alpha} + \sqrt{3}\alpha\Delta^*_t \psi'^\dagger_{i;\bar{\alpha}} , \tag{B16}$$

which is used in the Lehmann representation for the spectrum. In reality, the mean-field parameters B_s, Δ, Δ_t have their own fluctuations, and the real spectrum should be much broadened than our mean-field result.
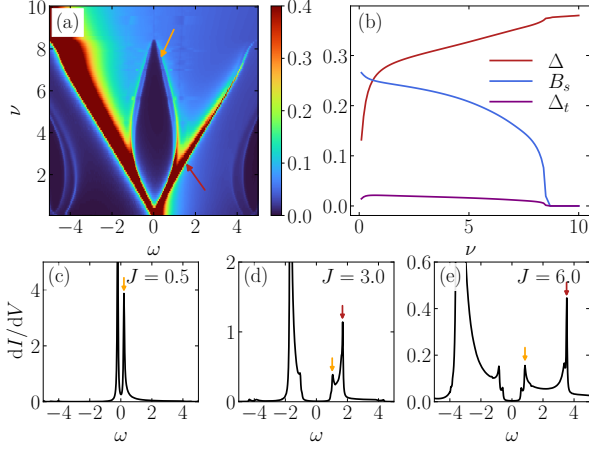

FIG. 5. Superconducting evolution as a function of spin coupling J when s-wave pairing is considered, for $\theta = 1.06°, w_0/w_1 = 0.8$, $U = 25$ meV, $M = 0$ and $\nu = -2.4$. (a) The STM spectrum and (b) the order parameters for different value of J. (c) (d) and (e) show three different line cuts of STM at $\nu = -2.9$, $\nu = -2.6$ and $\nu = -2.3$, respectively.
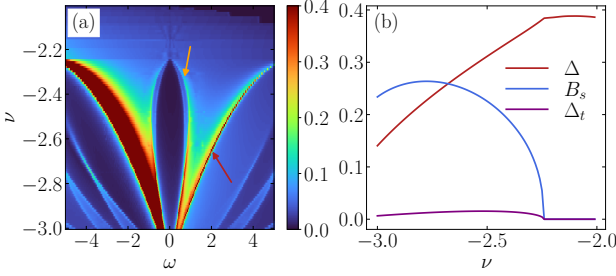

FIG. 7. Superconducting evolution as a function of charge density ν with a finite strain $\epsilon_{xy} = 3$ meV, for twist angle $\theta = 1.06°$, $w_0/w_1 = 0.8$, $U = 25$ meV, $J = 6$ meV and $M = 0$. (a) The STM spectrum and (b) the order parameters for different value of ν. (c) (d) and (e) show three different line cuts of STM at $\nu = -2.9$, $\nu = -2.6$ and $\nu = -2.3$, respectively.

FIG. 6. Superconducting evolution as a function of charge density ν when s-wave pairing is considered, for $\theta = 1.06°, w_0/w_1 = 0.8$, $U = 25$ meV $J = 6$ meV and $M = 0$. (a) The STM spectrum and (b) the order parameters for different value of ν.

Appendix C: More mean-field results

In this appendix, we show more mean-field results when different pairing channels are considered or when a finite strain is considered.

1. s-wave pairing channel

In the main text, we focus on the d-wave pairing states. However, s-wave pairing is also allowed within certain parameter regimes. Figs. 5 and 6 show the mean-field results at various doping levels and exchange couplings J when the s-wave pairing channel is considered. A char-
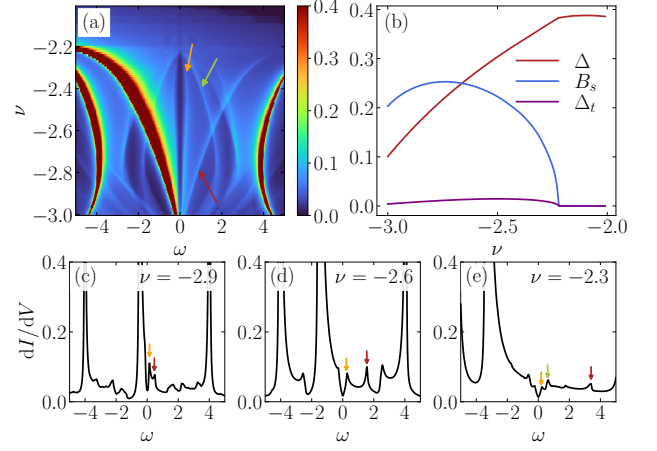
acteristic U-shaped superconducting gap appears in all cases, consistent with s-wave symmetry. The additional inter-band gap labeled by green arrow in Figs. 3 and 4 is absent here.

Despite the difference of the low energy SC gap, the high energy physics are essentially the same for both the s-wave and d-wave pairing channel. The two gap structure is also observed here. And the evolution of the order parameters, as well as the pseudogap size are almost the same as in the d-wave case. We therefore conclude that the RVB pairing mechanism based on an sFL is a more general framework which allows many different pairing channels. In principle, our framework also allows intra-valley pairing and pairing coexisting with IVC orders.

2. Effect of finite strain.

The ubiquitous effects of strain and lattice relaxation are important in TBG. In particular, Refs. [38, 41] have shown that within Hartree–Fock theory, the ground state evolves from a K-IVC to an IKS state when finite strain is included. Since the typical strain strength is considered comparable to the pseudogap energy scale, it is important to examine the stability of our results under finite strain.

To model the effect of heterostrain, we introduce a term that explicitly breaks lattice rotational symmetry,
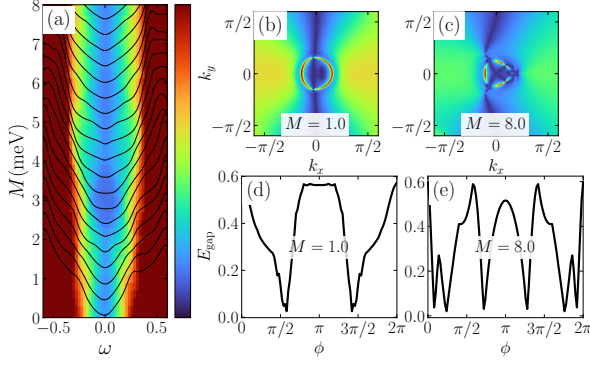
FIG. 8. Effect of the active band width M on the pairing symmetry. (a) STM spectrum as a function of M. For small and large M, the STM show a V shape SC gap with node. However, for intermediate value of $M \approx 3$ meV, there is a small gap in the spectrum. (b) and (c) show the gap function $|\Delta_{\mathrm{act};1}(\mathbf{k})|$ in the momentum space projected into one of the lower Hubbard band for $M = 1.0$ meV and $M = 8.0$ meV, respectively. (d) and (e) shows the minimal single particle gap along different azimuth angle ϕ for $M = 1.0$ meV and $M = 8.0$ meV.

$$H_\epsilon = \epsilon_{xy} \sum_{i,\eta,s} f^\dagger_{i;\eta+s} f_{i;\eta-s} + \text{h.c.} , \qquad (C1)$$

whose effect is treated exactly in the s–t subspace within our mean-field calculation. Its influence on the ψ' channel is neglected under the assumption that the J-term physics dominates.

Figure 7 presents the results for $\epsilon_{xy} = 3$ meV. The evolution of the order parameters remains nearly unchanged from the unstrained case. Both the superconducting gap and the pseudogap are suppressed by finite strain; the pseudogap, however, is more robust, while the superconducting gap becomes smaller but remains non-zero. A more detailed analysis shows that the superconducting gap is no longer nodal and acquires a small finite value $E_{\mathrm{gap}} \sim 0.01$ meV. This minor gap is not resolvable in the STM spectrum and does not alter the characteristic V-shape.

Appendix D: Analysis of the gap structure

1. Origin of the nematic nodal structure.

In this appendix, we give an analytical analysis of the nodal structure of the superconductor, and its dependence on the active band width M. We use the d-wave pairing ansatz for ψ'. Note that this pairing is still purely on-site and has no momentum dependence. In the SC phase with $B = 0$, the mobile carriers dominated by $s^\dagger$ inherit the pairing, so we expect on-site pairing term $\Delta(s_{i;+}s_{i;+} + s_{i;-}s_{i;-})$. Here we suppress the valley and
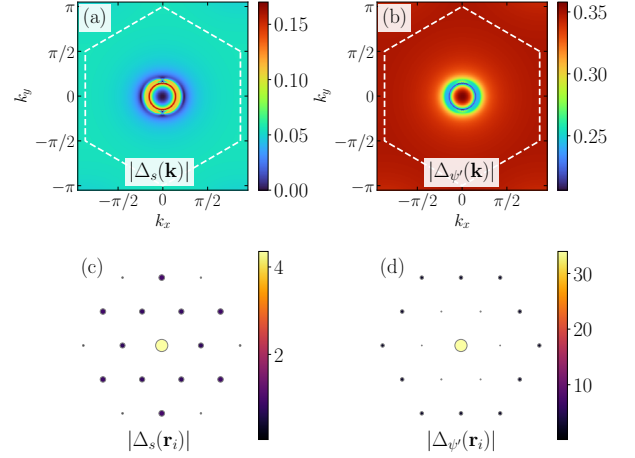

FIG. 9. The pairing order parameter (a) $\Delta_s(\mathbf{k}) = \alpha\langle s_{-\mathbf{k};\bar\alpha} s_{\mathbf{k};\alpha}\rangle$ for s fermion and (b) $\Delta_{\psi'}(\mathbf{k}) = \alpha\langle \psi'_{-\mathbf{k};\bar\alpha}\psi'_{\mathbf{k};\alpha}\rangle$ for ψ' fermion, calculated at twist angle $\theta = 1.06°$, $w_0/w_1 = 0.8$, $U = 25$meV, $J = 6$ meV and doping $x = 0.4$. Fourier transformed real space pairing for the (c) s fermion $\Delta_s(\mathbf{r}_i) = \frac{1}{\sqrt{N}}\sum_{\mathbf{k}}\Delta_s(\mathbf{k})e^{i\mathbf{k}\cdot\mathbf{r}_i}$ and (d) ψ' fermion $\Delta_{\psi'}(\mathbf{r}_i) = \frac{1}{\sqrt{N}}\sum_{\mathbf{k}}\Delta_{\psi'}(\mathbf{k})e^{i\mathbf{k}\cdot\mathbf{r}_i}$. Each circle represent an AA site of TBG. Here the s pair spread in the real space but ψ' pair is localized on a single AA site.

spin index. The pairing has no momentum dependence in the $(s_+(\mathbf{k}), s_-(\mathbf{k}))$ basis. However, we have two split Fermi surfaces due to the hybridization between s_+ and s_-, so the projected pairing to each split band acquires a momentum dependence. Therefore, it is important to understand the hybridization between s_+, s_- and the structure of the resulting Bloch wavefunction due to the hybridization.

We expect that the kinetic term of s just follows that of f. So in the following, we try to integrate c_1, c_2 to get an effective single-particle Hamiltonian for f. We focus on the regime where the Fermi surface momentum k_F is away from the Γ point such that the c_1, c_2 band energy $v_*|\mathbf{k}|$ is the largest energy scale. An estimation based on the current parameter $\gamma = -26.184$ meV and $U = 25$ meV shows that this condition is satisfied, except for the center 4.4% area of the mini Brillouin zone, corresponding to the doping level $x \sim 0.35$. Therefore, we can integrate out the c_1, c_2 fermion in Eq. (A1) for most of the regime where superconducting emerges. After integration, the f fermion gets an effective kinetic term :

$$H^{(f)}_{\mathrm{eff}} = \sum_{\mathbf{k}} f^\dagger_{\mathbf{k}} h_{\mathrm{kin}}(\mathbf{k}) f_{\mathbf{k}} + H^{(f)}_{\mathrm{int}} , \qquad (D1)$$

where

$$h_{\text{kin}}(\mathbf{k}) \approx \frac{1}{v^2|\mathbf{k}|^2}\gamma^\dagger(\mathbf{k})\begin{bmatrix}-\mu & Mk^2/|\mathbf{k}|^2 \\ M\bar{k}^2/|\mathbf{k}|^2 & -\mu\end{bmatrix}\tau_0 s_0 \gamma(\mathbf{k})$$
$$= \begin{bmatrix}\epsilon_{\text{kin}}(\mathbf{k}) & \delta_{\text{kin}}(\mathbf{k}) \\ \delta^*_{\text{kin}}(\mathbf{k}) & \epsilon_{\text{kin}}(\mathbf{k})\end{bmatrix}\tau_0 s_0 ,$$
(D2)

and

$$\epsilon_{\text{kin}}(\mathbf{k}) = \frac{e^{-|\mathbf{k}|^2\lambda^2}}{v^2|\mathbf{k}|^2}(-\mu\gamma_0^2 - \mu v'^2|\mathbf{k}|^2) , \qquad \text{(D3)}$$

$$\delta_{\text{kin}}(\mathbf{k}) = \frac{e^{-|\mathbf{k}|^2\lambda^2}}{v^2|\mathbf{k}|^2}(\gamma_0^2 Mk^2/|\mathbf{k}|^2 - 2\mu\gamma_0 v'\bar{k}) , \qquad \text{(D4)}$$

where we use the complex variable $k = k_x + ik_y$ and $\bar{k} = k_x - ik_y$. Here we keep only the most relevant first two terms for $\epsilon_{\text{kin}}(\mathbf{k})$ and $\delta_{\text{kin}}(\mathbf{k})$. The diagonal term $\epsilon_{\text{kin}}(k)$ is the dispersion generated by hybridizing with c_1, c_2, which disappears at the charge neutrality point $\mu = 0$. The off-diagonal term δ_{kin} is the effective mass term which splits the two orbitals. Due to $C_{2z}T$ symmetry, the σ_z mass term is forbidden.

Note that h_{kin} simply gives an effective dispersion for f orbital. Now we need to include the interaction $H^{(f)}_{\text{int}}$. In the doped Mott insulator at filling $\nu = -2 - x$, our interest lies in the lower Hubbard band, which is dominated by singlon s fermion when x is relatively large. Then the s fermion just inherits the effective kinetic term of the f orbital. The chemical potential now changes to around $\mu \sim -U/2$ due to the Hubbard interaction. Under the interaction, the diagonal term $\epsilon_{\text{kin}}(\mathbf{k})$ in Eq. (D3) now effectively raises the energy near the Γ point, producing an upward convex dispersion in the lower band near the Γ point. This is consistent with the band structure shown in the right inset of Fig. 1 (a).

For the band-splitting mass term $\delta_{\text{kin}}(\mathbf{k})$ in Eq. (D4), the two distinct terms exhibit qualitatively different angular dependencies. The first contribution, characterized by the active bandwidth M, produces a vortex structure of the Bloch wavefunction which winds twice, $\sim e^{2i\phi(\mathbf{k})}$, as $\mathbf{k}$ encircles around each of the two Fermi surfaces. This would lead to a superconductor with two nodal lines at each Fermi surface.

The second contribution is proportional to the chemical potential $\mu \sim -U/2$, and displays a p-wave–like angular dependence $\sim e^{-i\phi(\mathbf{k})}$. It gives rise to a single nodal line in the superconductor. Basically, along the direction of $\phi = \pm\frac{\pi}{2}$, the pairing projected on the band basis vanishes. Both contributions are symmetry-allowed under the C_{3z} rotation of TBG, with the first term more important around the Γ point with small doping and the second term more important away from the Γ point with larger doping. However, the second term is driven purely by interaction and therefore dominates over the first term when M is small. Therefore, we expect a single nodal line in the superconductor.

2. Effect of bandwidth M.

In Fig. 8 we show the STM spectrum for $w_0/w_1 = 0.8$, $\theta = 1.06°$, $J = 6$ meV, $U = 25$ meV, but with the active band width varying from $M = 0$ to $M = 8$ meV. A nodal SC structure is seen for both a very small M, and a very large M. The pairing structure is very different in the two regimes. For $M \approx 0$, the superconductor gap along each Fermi surface is p_x-wave like. For $M \approx 8$ meV, the superconductor gap has two nodal lines and is similar to $d_{x^2-y^2}$ pairing.

In the intermediate regime around $M \approx 3$ meV, the two hybridization terms compete with each other and the resulting STM spectrum shows no node. We note that even when the spectrum is not totally gapless, the gap is still momentum dependent, and it may still look like a V-shape in the STM spectrum.

3. Comparison between the local pairing and the superconducting pairing.

In Fig. 9, we show the momentum- and real-space pairing order parameters for both the mobile hole s and netural spinon ψ' fermions. For the s fermion, the pairing amplitude $\Delta_s(\mathbf{k})$ is concentrated near the Fermi surface, leading to a broader distribution in real space $\Delta_s(\mathbf{r}_i) = \frac{1}{\sqrt{N}}\sum_\mathbf{k}\Delta_s(\mathbf{k})e^{i\mathbf{k}\cdot\mathbf{r}_i}$. In contrast, the ψ' fermion exhibits nearly uniform pairing in momentum space, with only weak $\mathbf{k}$ dependence near the Fermi surface. This corresponds to a localized pairing of ψ' within a single AA site in real space. The superconductivity is mainly driven by pairing of the mobile hole s fermions, and the cost of Hubbard U is reduced because of its finite size in real space. Note that there is still a large on-site component, which is the artifact of the mean field calculation. In a more rigorous variational Monte Carlo (VMC) calculation using a Gutzwiller projected wavefunction to impose the constraint $n_{i;s} + n_{i;t} + \frac{1}{2}n_{i;\psi'} = 1$ exactly, this on-site contribution for pairing of s would be removed.

Appendix E: Gauge theory and confinement in the sFL phase

In this section we discuss the gauge structure of our parton construction. We note that in the superconductor (SC) and FL phase, all of the internal gauge fields are simply higgsed, so we do not need to worry about them. But the sFL phase needs some careful discussion. Our parton construction is as follows:

$$f_{i;\alpha} = \sum_\beta s^\dagger_{i;\beta}\psi'_{i;\beta}\psi'_{i;\alpha} + \sum_{\beta\gamma} t_{i;\alpha\beta\gamma}\psi'^\dagger_{i;\beta}\psi'^\dagger_{i;\gamma} , \qquad \text{(E1)}$$

Then there is an internal U(1) gauge field a_μ associated with the local gauge transformation: $\psi'_{i;\alpha} \rightarrow$

$\psi'_{i;\alpha}e^{i\varphi_i}$, $s_{i;\alpha} \to s_{i;\alpha}e^{i2\varphi_i}$, $t_{i;\alpha\beta\gamma} \to t_{i;\alpha\beta\gamma}e^{i2\varphi_i}$. We also introduce a probing field A_μ for the physical U(1) gauge field which generates the electric and magnetic field in physical world. In the end, s couples to $-A_\mu + 2a_\mu$, t couples to $A + 2a_\mu$ and ψ' couples to a_μ. We interpret ψ' as a neutral spinon, similar to the widely used Abrikosov fermion.

In the FL phase, we condense a slave boson $B \sim f_\alpha^\dagger \psi'_\alpha$, which couples to $-A_\mu + a_\mu$. After the condensation of this Higgs boson B, we have $a_\mu = A_\mu$. Then the neutral spinon ψ' is now charged under the physical U(1) field and has a finite spectral weight.

On the other hand, in the sFL phase, we have $\langle B \rangle = 0$. Instead, we condense the spinon pairing term $\Delta \sim \psi_\alpha \psi_\beta$. For now let us ignore the flavor dependence. Note that Δ couples to $2a_\mu$ and its condensation only higgses the U(1) internal gauge field down to Z_2. Therefore, in our current ansatz of sFL phase, there is still a remaining Z_2 gauge field. We always have $f_i \sim s^\dagger \sim t$, so s and t now have finite overlap with the physical hole and electron operator. If the remaining Z_2 gauge field does not confine, we should call the phase fractionalized Fermi liquid (FL*)[70] because there is a hidden topological order. However, in 2+1d, Z_2 gauge field can be confined into a trivial and symmetric phase by condensing a vison (π flux of the gauge field a_μ) if the vison does not carry a non-trivial quantum number under symmetry. For the usual case of an odd Mott insulator with one electron per site, vison always carries a momentum which forbids its condensation into a symmetric phase. However, in our case, we have two electrons in the Mott insulator, and the vison does not have any quantum number. So both deconfined and confined phases are possible[71], depending on energetics. At $\nu = -2$, they correspond to a Z_2 spin liquid and a trivial 'rung singlet' phase.

From our understanding, the local moments at $\nu = -2$ should just form a trivial and featureless 'rung singlet' phase, so in this work we always assume that the Z_2 gauge field is confined. Such a confinement should persist near the sFL to SC transition. In the sFL phase, B couples to $-A_\mu$ and the Z_2 gauge field. Given the Z_2 gauge field is confined, at the sFL-SC transition, the slave boson B is confined and the transition should be driven by the phase coherence of a pair of B, which couples to $-2A_\mu$ and can be identified as a physical Cooper pair. Thus in the long distance limit, the sFL to SC transition should also be in the BKT universality class. It would be interesting to study whether the slave boson B can be probed in the short distance, such as in the core of the vortex of the superconductor.